

Non-reflecting boundary flux function for finite volume shallow-water models

Brett F. Sanders

Department of Civil and Environmental Engineering, University of California, Irvine, CA 92697, USA

Received 28 August 2000; accepted 15 May 2001

Abstract

An approach to implement non-reflecting boundary conditions in finite-volume based shallow-water models is presented. Shallow-water models are routinely applied to sections of rivers, estuaries, and coastal zones, introducing computational boundaries where no physical control is present, and necessitating a condition that supplies information to the model while it simultaneously allows disturbances from the interior to pass out unhampered. The approach presented here builds upon the finite-volume convention of constructing a Riemann problem at the interface between cells and then solving it with a flux function. Hence, non-reflecting boundary conditions are achieved using a non-reflecting flux function on cell faces aligned with open boundaries. Numerical tests show that the non-reflecting flux function performs extremely well when waves advance toward the boundary with a small incident angle (approximately less than 45° from the boundary normal direction), while very minor reflections are present when the incident angle is larger. The presence of minor reflections, when the incident angle is large, is consistent with non-reflecting conditions previously implemented in finite-difference based schemes. © 2002 Elsevier Science Ltd. All rights reserved.

1. Introduction

Shallow-water models of river and estuarine systems are routinely applied on limited spatial domains. That is, the domain is not completely defined by physical boundaries such as shoreline or a control section. As a result, model boundaries are placed at arbitrary inflow and outflow sections. It is necessary to specify either the discharge, the depth, both, or none at these open boundaries depending on the Froude number [1]. Under subcritical flow conditions, non-physical reflections will occur at open boundaries where either the depth or discharge is specified, unless a procedure is implemented to achieve non-reflecting boundaries [2]. Non-reflecting boundaries, sometimes called *absorbing* or *partially reflecting* boundaries, allow disturbances generated within the solution domain to pass through the model boundary unhampered, while information from outside the solution domain is simultaneously specified to achieve the desired interior solution.

There has been growing interest in finite-volume based schemes in recent years for shallow-water wave computations, particularly for the computation of

surges and shocks [3–10]. However, finite-volume models have also proven useful in coastal applications such as long wave run-up on a beach and tidal inundation of wetlands [11,12]. In these latter applications, non-reflecting boundary conditions are essential for an accurate depiction of flow because limited spatial domains are commonplace.

The theoretical basis for non-reflecting boundary conditions in shallow-water models is well developed [2,13]. The general idea is to introduce a constraint that allows Riemann variables moving along outward-bound characteristics to leave the domain unhampered, while information is simultaneously supplied to the solution domain by the Riemann variables moving along inward-bound characteristics. However, this approach can be challenging to implement in models based on the finite-difference method, particularly in the presence of bed resistance. At the boundary, compatibility equations must be solved along the bicharacteristics of the characteristic conoid, the surface that connects the solution at the update $(n+1)$ time level to that at the base (n) time level [14]; and this procedure is awkward when conventional finite-difference stencils are used. Furthermore, stability limitations associated with the treatment of bed resistance terms can arise [13]. Models based on a Godunov-type finite-volume method, on the

E-mail address: bsanders@uci.edu (B.F. Sanders).

other hand, are ideally suited for the implementation of non-reflecting boundary conditions because Riemann problems are solved at each cell face over an infinitesimal length. Therefore, bicharacteristics are perfectly captured by straight lines and the integration of friction terms at the cell face is not necessary. In this paper, we present a simple flux function for open boundaries of finite-volume models that can be used to minimize, and in some cases eliminate, non-physical reflections while simultaneously introducing information to the solution domain.

2. Background

The shallow-water equations are a system of quasi-linear hyperbolic conservation laws and therefore can be written in integral form as

$$\frac{\partial}{\partial t} \int_{\Omega} \mathbf{U} d\Omega + \oint_{\partial\Omega} (\mathbf{F} dy - \mathbf{G} dx) = \int_{\Omega} \mathbf{S} d\Omega \quad (1)$$

with

$$\mathbf{U} = \begin{pmatrix} h \\ uh \\ vh \end{pmatrix}, \quad \mathbf{F} = \begin{pmatrix} uh \\ u^2h + \frac{gh^2}{2} \\ uvh \end{pmatrix},$$

$$\mathbf{G} = \begin{pmatrix} vh \\ uvh \\ v^2h + \frac{gh^2}{2} \end{pmatrix}, \quad \mathbf{S} = \begin{pmatrix} 0 \\ gh \left(\frac{\partial z_b}{\partial x} + S_f^x \right) \\ gh \left(\frac{\partial z_b}{\partial y} + S_f^y \right) \end{pmatrix},$$

where Ω is an arbitrary spatial domain, z_b is the elevation of the bed, and S_f^x and S_f^y are the friction slopes in the x - and y -directions, respectively. The friction slopes are commonly evaluated using the well-known Manning formula as follows [1]:

$$S_f^x = \frac{n^2 u \sqrt{u^2 + v^2}}{h^{4/3}}, \quad S_f^y = \frac{n^2 v \sqrt{u^2 + v^2}}{h^{4/3}}. \quad (2)$$

Initial conditions for \mathbf{U} as well as boundary conditions are required to solve (1). At shoreline boundaries, the component of the fluid velocity normal to the boundary is set to zero, while at open boundaries the condition depends on the Froude number. For $Fr > 1$, \mathbf{U} is completely specified at inflow boundaries and completely unspecified at outflow boundaries. For $Fr < 1$, \mathbf{U} is not completely specified. Of the three degrees of freedom in \mathbf{U} , the number that are specified is given by the number of characteristics entering the solution domain. Two characteristics enter the domain at a subcritical inflow boundary, while one enters at a subcritical outflow boundary. Hence, the discharges $p = uh$ and $q = vh$ are generally specified at inflow boundaries, while the depth is specified at outflow boundaries. In the limit of steady flow, this creates the proper constraints to achieve a gradually varied flow profile [15]. The key to implementing non-reflecting boundary conditions is the

specification of either the discharge or the depth at an open boundary such that disturbances generated within the solution domain pass outwards unhampered.

The finite-volume method is predicated on the direct discretization of the integral equations given by (1), in contrast to the discretization of the associated differential equations. This leads to conservation properties that are superior to finite-difference schemes, as well as a scheme that remains accurate in the presence of surges and shocks [16]. Here, (1) is directly discretized as

$$\Omega \frac{(\mathbf{U}^{n+1} - \mathbf{U}^n)}{\Delta t} - (\mathbf{F}_{\perp})_1^{n+1/2} \Delta s_1 + (\mathbf{F}_{\perp})_2^{n+1/2} \Delta s_2 \\ + (\mathbf{F}_{\perp})_3^{n+1/2} \Delta s_3 - (\mathbf{F}_{\perp})_4^{n+1/2} \Delta s_4 = \mathbf{Z}^{n+1/2}, \quad (3)$$

where Ω has been taken to be a quadrilateral cell. The quantities in \mathbf{U} are defined to be the cell (spatial) averages, $\mathbf{F}_{\perp} = \mathbf{F} \cos \alpha + \mathbf{G} \sin \alpha$ is the flux perpendicular to each cell face evaluated at the half $(n + 1/2)$ time level, α is the angle between the face normal and the x axis, and \mathbf{Z} represents the numerical discretization of the source terms. The subscripts in (3) denote the faces of the cell and Δs is the cell face length. The subscript “1”, for example, denotes the bottom cell face while the others are numbered in a counter-clockwise manner.

The flux \mathbf{F}_{\perp} is evaluated at the half-time level to achieve second-order temporal accuracy, and the Monotone Upwind Scheme for Conservation Laws (MUSCL) approach is used to achieve second-order spatial accuracy [17]. This combination of schemes has been employed by numerous researchers to achieve a solution to the shallow-water equations that is monotone and second-order accurate in both space and time [8–12], and it has also been used to solve equations of analogous form that describe turbidity current hydrodynamics [18].

Finite-volume schemes that utilize the MUSCL approach assume that the solution is piece-wise linear. Therefore, a discontinuity may exist at each cell face with \mathbf{U}_L and \mathbf{U}_R representing the solution on the left and right sides of the face, respectively. Two states initially separated by a barrier and subsequently allowed to interact constitute a Riemann problem. Godunov-type schemes solve this Riemann problem at every cell face to give the interface flux \mathbf{F}_{\perp} needed to update the solution.

2.1. Roe's Riemann solver

A widely used Riemann solver is Roe's scheme. It gives the flux as follows: [19],

$$\mathbf{F}_{\perp} = \frac{1}{2} (\mathbf{F}_{\perp}^L + \mathbf{F}_{\perp}^R - \hat{\mathbf{R}} |\hat{\Lambda}| \hat{\Delta \mathbf{V}}), \quad (4)$$

where $|\hat{\Lambda}|$ is the diagonal matrix containing the absolute values of the eigenvalues of the Jacobian of \mathbf{F}_{\perp} , and the columns of $\hat{\mathbf{R}}$ contain the corresponding right eigenvectors. In addition, $\hat{\Delta \mathbf{V}} = \hat{\mathbf{R}}^{-1} \Delta \mathbf{U}$ represents the finite

difference in characteristic variables between the right and left states, and $\mathbf{F}_\perp^L = \mathbf{F}_\perp(\mathbf{U}^L)$ and $\mathbf{F}_\perp^R = \mathbf{F}_\perp(\mathbf{U}^R)$ represent the fluxes associated with the left and right states, respectively. Finally the hat notation appearing in (4) implies that Roe averages be used to evaluate the eigenvalues and eigenvectors at the cell face. The matrix of eigenvalues, right eigenvectors, and characteristic variables are given, respectively, as

$$|\hat{\mathbf{A}}| = \begin{pmatrix} |\hat{u}_\perp - \hat{a}| & 0 & 0 \\ 0 & |\hat{u}_\perp| & 0 \\ 0 & 0 & |\hat{u}_\perp + \hat{a}| \end{pmatrix}, \quad (5)$$

$$\hat{\mathbf{R}} = \begin{pmatrix} 1 & 0 & 1 \\ \hat{u} - \hat{a} \cos \alpha & -\sin \alpha & \hat{u} + \hat{a} \cos \alpha \\ \hat{v} - \hat{a} \sin \alpha & \cos \alpha & \hat{v} + \hat{a} \sin \alpha \end{pmatrix} \quad (6)$$

and

$$\Delta \hat{\mathbf{V}} = \begin{pmatrix} \frac{1}{2}(\Delta h - \frac{\hat{h}\Delta u_\perp}{a}) \\ \hat{h}\Delta u_\parallel \\ \frac{1}{2}(\Delta h + \frac{\hat{h}\Delta u_\perp}{a}) \end{pmatrix}, \quad (7)$$

where $u_\parallel = -u \sin \alpha + v \cos \alpha$ is the velocity parallel to the cell face. Hirsch [16] presents additional detail on Roe's approximate Riemann solver when applied to the Euler equations describing compressible gas dynamics. Glaister [20] presents Roe's solver when applied to the shallow-water equations in one dimension.

Roe's flux function is robust. It recognizes both expansion waves and shock waves. Although it will incorrectly interpret a critical flow point within an expansion wave as a shock wave, this error can easily be corrected [21].

2.2. Simplified Riemann solver

When the flow is known a priori to be subcritical, which is the case when non-reflecting boundary conditions are needed, a simplified flux function can be used on cell faces aligned with open boundaries. The simplified flux function is valid only in the absence of discontinuous flow, unlike Roe's method above. Nevertheless, open boundaries in river and estuarine models are rarely placed at locations where discontinuities (surges and shocks) occur. Regions where these flow features are present should be encompassed by the model domain.

Using this approach, the interface flux is obtained by interpreting the Riemann problem as the interaction of two simple waves (i.e., waves with straight-line characteristics). The left state sends $R^+ = u_\perp + 2a$ forward across the cell face, the right state sends $R^- = u_\perp - 2a$ backward across the cell face, and the third Riemann variable, $R^\circ = u_\parallel$, is advected by u_\perp . Based on these Riemann variables, the interface velocities and depth are computed as follows:

$$(u_\perp)_I = \frac{1}{2}(R_L^+ + R_R^-), \quad (8)$$

$$(u_\parallel)_I = \{R_L^\circ \text{ if } (u_\perp)_I > 0, \quad R_R^\circ \text{ if } (u_\perp)_I < 0\}, \quad (9)$$

$$(h)_I = \frac{1}{16g}(R_L^+ - R_R^-)^2. \quad (10)$$

Then, interface values of u and v are recovered from u_\perp and u_\parallel as follows:

$$(u)_I = (u_\perp)_I \cos \alpha - (u_\parallel)_I \sin \alpha, \quad (11)$$

$$(v)_I = (u_\perp)_I \sin \alpha + (u_\parallel)_I \cos \alpha. \quad (12)$$

Finally, the interface flux is given by

$$\mathbf{F}_\perp = \begin{pmatrix} u_\perp h \\ uu_\perp h + \frac{gh^2}{2} \cos \alpha \\ vu_\perp h + \frac{gh^2}{2} \sin \alpha \end{pmatrix}_I. \quad (13)$$

3. Implementation of non-reflecting boundary conditions

The simplified flux function calls for values of Riemann variables on opposing sides of boundary cell faces. This necessitates the specification of the inward-bound Riemann variables. In practice, however, it is more common to specify the discharge or depth. Therefore, the inward-bound Riemann variables must be computed based on the desired discharge or depth. Using the outward-bound Riemann variables computed from the interior side of the boundary cell face and the inward-bound Riemann variables computed from the desired depth or discharge, the interface flux is computed using (8)–(13). Once \mathbf{F}_\perp is evaluated, the boundary cell solution can be updated by (3) and the desired physical behavior will be achieved at the boundary. The steps necessary to evaluate the inward-bound Riemann variables are described below.

3.1. Inflow boundary

At an inflow boundary, the discharge per unit width is customarily specified as, $p = p^*$ and $q = q^*$, where p^* and q^* are arbitrary functions of position along the boundary and time. In this case, R_R^- is evaluated from the solution at the interior side of the boundary cell face, and R_L^+ and R_L° are evaluated from p^* and q^* . (By convention, we assume that the interior of the domain at an inflow boundary is the R side and the exterior is the L side. The opposite is assumed for an outflow boundary.) Based on (8) and (10)

$$(q_\perp)_I = \frac{1}{32g}(R_L^+ - R_R^-)^2(R_L^+ + R_R^-). \quad (14)$$

By setting $(q_\perp)_I = p^* \cos \alpha + q^* \sin \alpha$, (14) can be used to solve for R_L^+ given R_R^- . Recognizing that the boundary must allow disturbances to pass, the discharge at the

boundary must deviate from $(q_{\perp})_I$ in the presence of disturbances. Therefore, R_L^+ is computed from (14) given that R_R^- is an undisturbed interior state U_U . (14) then becomes,

$$p^* \cos \alpha + q^* \sin \alpha = \frac{1}{32g} (R_L^+ - (R_R^-)_U)^2 (R_L^+ + (R_R^-)_U), \quad (15)$$

which is a cubic equation in R_L^+ . The desired value is given by the positive-definite root. Here, $(R_R^-)_U$ indicates that U_U is used to evaluate R_R^- . The undisturbed reference state, U_U should be selected as the value of U at the boundary when $t = 0$, the initial condition. Physically, this state corresponds to the flow conditions prior to the arrival of disturbances from other boundaries. This procedure for evaluating R_L^+ ensures that the desired discharge will be specified at the boundary in the absence of disturbances, and that the necessary change in discharge at the boundary will occur in the presence of disturbances such that reflections do not occur.

Using R_L^+ computed from (15) and R_R^- computed from the interior of the boundary cell face, the interface values of h , u and v follow directly from (8)–(12), and these can be substituted into (13) to obtain the corresponding boundary flux vector.

3.2. Outflow boundary

At an outflow boundary, the depth is conventionally specified as $h = h^*$, where h^* is an arbitrary function that varies with position along the boundary and time. In this case, (8)–(10) are solved under the condition that R_L^+ and R_L^o are evaluated from the solution at the interior side of the boundary cell face, and R_R^- is evaluated from h^* . R_R^- is evaluated using (10) under the condition that $h_1 = h^*$ and $R_L^+ = (R_L^+)_U$, where $(R_L^+)_U$ is the value of R_L^+ associated with an undisturbed state U_U that is given by the value of U at $t = 0$. Hence, R_R^- is given by

$$R_R^- = (R_L^+)_U - 4\sqrt{gh^*}. \quad (16)$$

Once R_R^- is computed from (16) and R_L^+ is computed from the interior side of the boundary cell face, the interface values of h , u and v again follow directly from (8)–(12).

3.3. Soft boundary

A soft boundary condition allows information to freely pass through a boundary, but it does not allow information to simultaneously be specified to drive the solution on the domain interior. This amounts to an extrapolation technique that can be useful in some applications.

Soft boundaries are implemented using ghost cells that line the outer edge of the domain. The solution in

the ghost cell is extrapolated based on the solution in adjacent interior cells, and a flux function is then executed to obtain the mass and momentum fluxes at the boundary. The simplest form of extrapolation sets the ghost cell solution equal to the interior cell solution, i.e., $U_g = U_d$. Higher order extrapolations are also sometimes used. The two primary disadvantages of using soft boundary conditions are: (a) that outside information cannot enter the solution domain, possibly creating an ill-posed problem, and (b) extrapolation at the boundary can create numerical instabilities. The primary advantages of the soft boundary are ease of use and compatibility with the flux function used at interior cell faces.

4. Test simulations

The performance of the non-reflecting boundary conditions described above is examined using a series of computational tests. First, we consider a problem described completely in one-dimension, so velocity terms and gradients in the y -direction are dropped from the model given by (1). The problem involves flow in a wide rectangular channel with a length $L = 1000$ m, a constant slope $S_0 = -dz_b/dx = 0.0001$, and a Manning coefficient of $n = 0.02$. Initially, flow is uniform at a depth of $h_1 = 2.0$ m and velocity $u_1 = (1/n)h_1^{2/3}S_0^{1/2}$ (0.7937 m/s).

At the upstream and downstream boundaries, the discharge and depth, respectively, are specified such that monotonic waves enter the channel and propagate towards the opposite end. The discharge is specified at the upstream boundary as

$$q(x = 0, t) = u_1 h_1 + 1.0 \operatorname{sech}(0.03(t - 120)), \quad (17)$$

while the depth is specified as

$$h(x = L, t) = h_1 + 0.2 \operatorname{sech}(0.03(t - 120)). \quad (18)$$

In Fig. 1, the depth as a function of distance along the channel (x) and time (t) is plotted. Here, the initial condition corresponds to the rear of the surface, the specified discharge boundary condition corresponds to the left side of the surface, and the specified depth boundary condition corresponds to the right side of the surface. Hence, the forward time direction is from back to front. Tracking the evolution of the solution from back to front, it is clear that elevation waves enter the domain roughly at $t = 120$ s and propagate towards opposite ends of the channel. When the waves cross each other at the center of the channel, the depth is a maximum. What is particularly important to note here, however, is the behavior of the waves upon reaching the opposite ends of the channel. Specifically, the waves pass through the boundary without even a minor reflection, even though either the depth or discharge is specified.

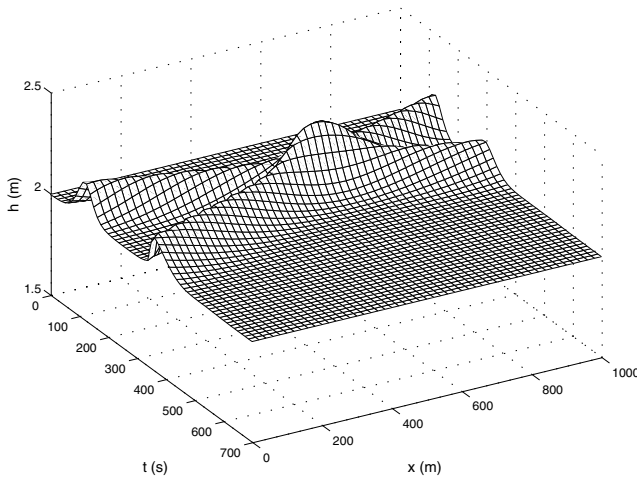


Fig. 1. Depth plotted as a function of distance along the channel, x , and time, t . Waves are specified simultaneously at $x = 0$ and $x = 1000$ m and pass unreflected through the opposite end of the channel.

The reality is that, while boundary condition at $x = 0$ calls for the discharge to be approximately $u_1 h_1$ at $t \approx 400$ s, it is not. Upon detecting the outgoing wave, the non-reflecting flux function leads to a discharge that is different from what is specified. The situation is analogous at the downstream boundary. While the boundary condition calls for a depth of approximately h_1 at $t \approx 300$ s, the actual depth is greater than this ($h \approx 2.15$ m) to allow the outgoing wave to leave.

While an outgoing wave is passing through the boundary, the non-reflecting flux function is still able to supply the solution domain with correct wave information. For example, consider the situation that arises when one wave is specified at a boundary while another wave is simultaneously passing through (outward direction) the boundary. This situation is created by repeating the previous test but with the downstream depth specified as

$$h(x = L, t) = h_1 + 0.2 \operatorname{sech}(0.03(t - 300)). \quad (19)$$

The depth as a function of distance along the channel (x) and time (t) is plotted for this case in Fig. 2. The interaction of the two waves now takes place at the downstream boundary (right side of surface), whereas the wave interaction took place in the center of the channel in the previous test. Nevertheless, an upstream signal consistent with the downstream boundary condition emerges from the wave interaction. This signal takes on a shape that appears identical to the upstream moving signal in Fig. 1, only the former is offset in time from the latter.

These tests illustrate how the non-reflecting boundary condition procedures presented here allow information to be supplied to the solution domain, while interior disturbances pass outwards unhampered, even in the presence of substantial bed resistance ($n = 0.02$).

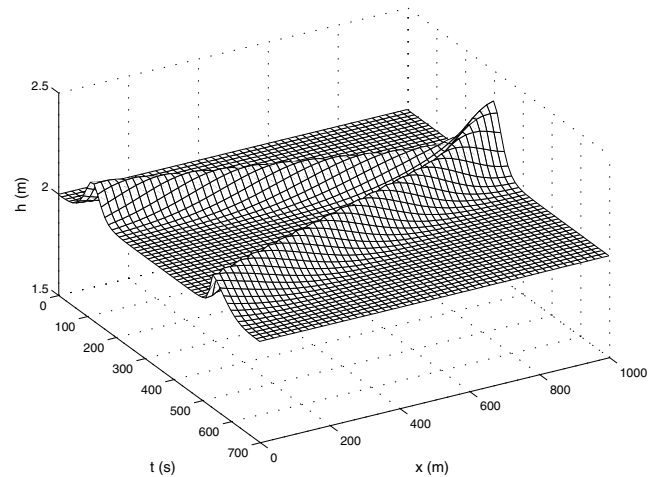


Fig. 2. Depth plotted as a function of distance along the channel, x , and time, t . Wave is specified at downstream boundary while wave from upstream boundary is exiting. Note that the emergent upstream-moving wave is nearly identical to that appearing in Fig. 1, only it is offset in time.

Next, the performance of this approach is examined in two-dimensional problems. These represent a much more stringent test of the method, since the characteristic decomposition inherent to the procedure models omni-directional wave propagation with locally bi-directional (1D) mathematics. That is, the characteristic decomposition is performed along the direction of the cell face normal vector.

In the first two-dimensional problem, water is initially at rest at a depth of $h_1 = 1$ m in an infinitely large channel bed with a Manning coefficient $n = 0.02$, except in a circular area of diameter $D = 10$ m at the center of the domain, where water rests at a level of 2 m. Beginning at $t = 0$, the elevated water column is allowed to interact with the surrounding fluid, and waves propagate radially outwards away from the center of the domain. This wave action is modeled in three separate ways: (1) on a small grid using the non-reflecting boundary condition that specifies a depth of $h^* = 1$ m on all sides, (2) on a small grid using a soft boundary condition on all sides, and (3) on a large grid. The small grid is given by a square domain of length 200 m discretized by 61 cells in each direction, while the large grid is given by a square domain of length 600 m discretized by 183 cells in each direction. A sketch of the domains used here are presented in Fig. 3. This test is repeated using an initially elevated region that is off-center, as is noted in Fig. 3. A uniform time-step of $dt = 0.1$ s is used in all cases.

The solution on the large grid serves as a control by which the performance of the solutions on the small grid can be measured. The time-history of the free surface level $\eta = h - h_1$ at six monitoring stations predicted by the small grid and large grid cases are presented in Fig. 4

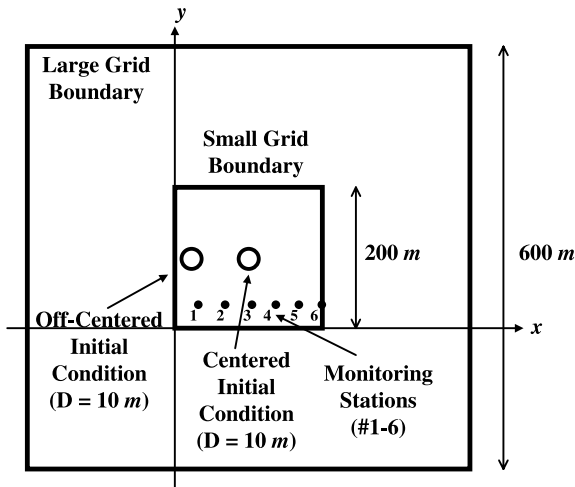


Fig. 3. Spatial domain of computational grid and location of monitoring stations.

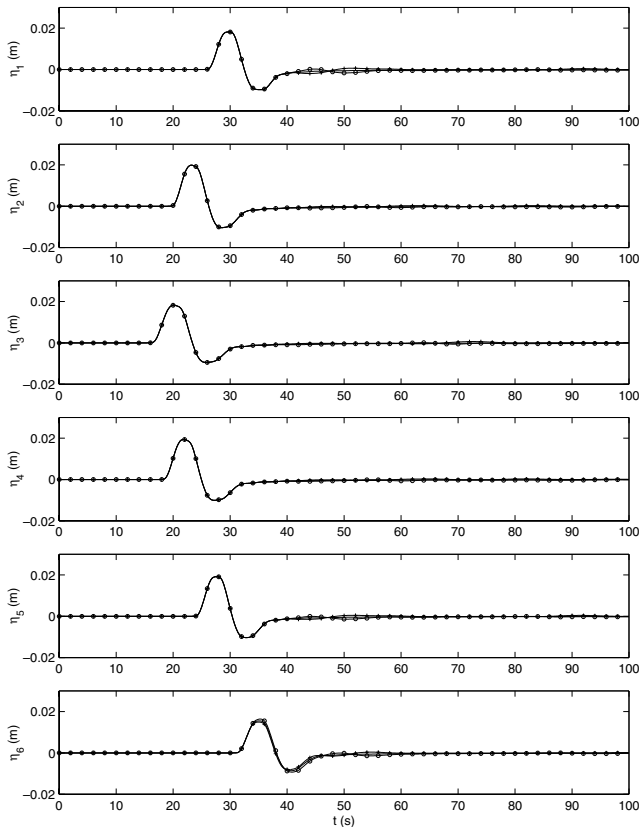


Fig. 4. Surface elevation at monitoring stations 1–6 predicted with large grid (solid line), non-reflecting condition on small grid (line with crosses), and soft condition on small grid (line with circles) resulting from the centered initial condition. Note that all three lines are essentially congruous.

for the centered initial condition problem and Fig. 5 for the off-centered initial condition problem. The monitoring stations are located along $y = 31.147$ m (the 10th row of cells above the lower small grid boundary) and

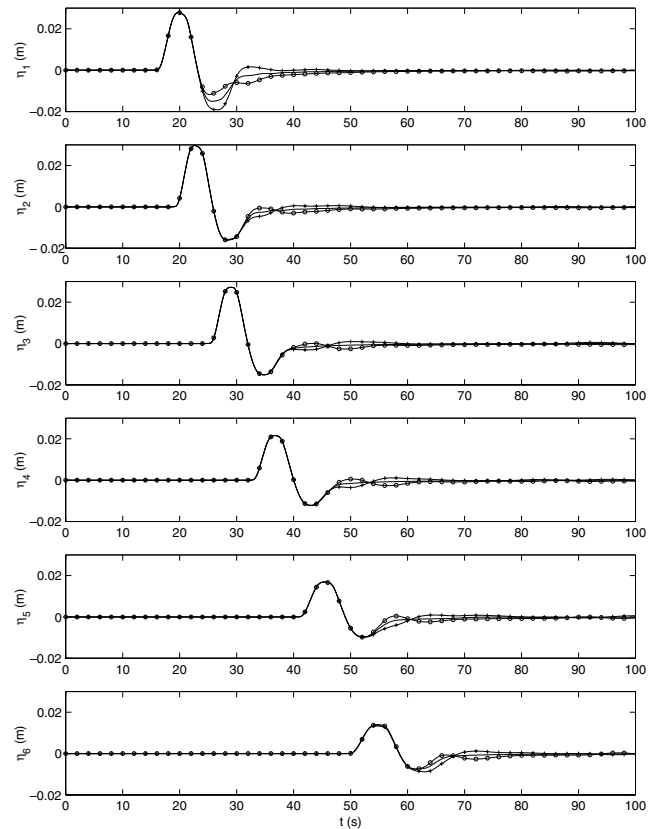


Fig. 5. Surface elevation at monitoring stations 1–6 predicted with large grid (solid line), non-reflecting condition on small grid (line with crosses), and soft condition on small grid (line with circles) resulting from off-centered initial condition. Note small reflections at tail of wave resulting from larger incident angles between advancing wave and boundary normal.

are spaced 33.333 m apart along the x -direction, as is shown in Fig. 3. The prediction associated with the large grid is given by the solid line, the prediction associated with the non-reflecting boundary condition and the small grid is given by the line marked with crosses, and the prediction associated with the soft boundary condition and the small grid is given by the line marked with circles.

Comparing the three predictions for both the centered and off-centered cases, several issues are made clear. First, the non-reflecting and soft boundary conditions predict the wave propagation through the boundary nearly perfectly for the case of a centered initial condition. Careful inspection of Fig. 4 shows that the soft-boundary and non-reflecting predictions only slightly deviate from the control (large grid) prediction at stations 1, 5, and 6. (Time histories at Stations 1 and 5 are identical due to the symmetry of the problem, as are Stations 2 and 4.) Second, reflections in the small-grid predictions are detectable, but small, for the case of the off-centered initial condition as is shown in Fig. 5. Third, the two small-grid predictions are not the same.

The reflectance of non-reflecting boundaries is proportional to the angle between the incident wave and the boundary outward normal vector [12]. In the centered case, the incidence angle is at most 45° (at the corners of the grid), while in the off-centered case, larger incidence angles exist. Hence, the increase in reflectance associated with the off-centered case is a result of larger incidence angles. While the non-reflecting flux function is not perfect, the small reflections that do arise are acceptable for most practical applications of shallow-water models.

To demonstrate the application of non-reflecting boundary conditions in a more practical setting, we consider a scenario motivated by the desire to predict long-wave resonance phenomena in harbors. Most harbors are protected from short-waves by breakwaters, but long-waves with periods $O(10^2 \text{ s})$ can pass directly through many outer breakwaters and disturb harbor operations [22]. Numerical models capable of predicting resonance phenomena can be useful for designing wave dampening strategies.

We consider a rectangular harbor slip that is 1 km in length and width, square to the ocean, and 10 m deep, as is shown in Fig. 6. In the model, the ocean floor slopes downward in the seaward direction over 1 km to a flat shelf with a depth of 20 m. The harbor is subjected to sinusoidal long-waves that pass the 20 m shelf at a 30° angle from the shoreline normal direction. The wave period and amplitude is $T = 50 \text{ s}$ and $A = 0.1 \text{ m}$, respectively. In addition, a long-shore current with a magnitude of 0.1 m/s is directed in the up-coast direction in the model. Note that a conforming grid is used to align the off-shore boundary with the incoming waves.

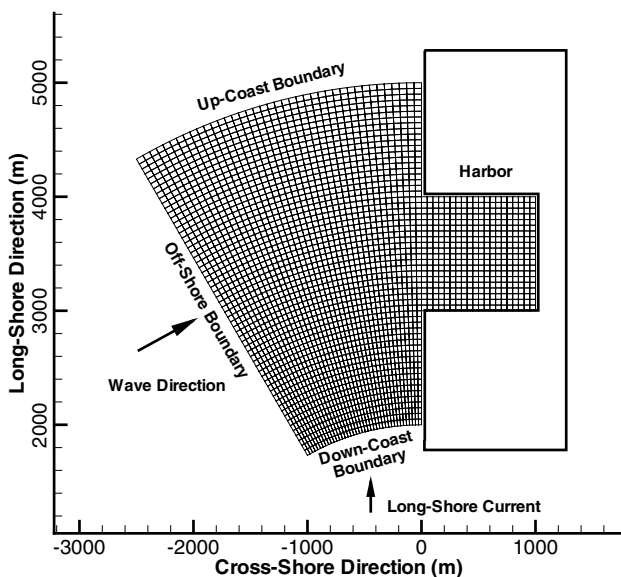


Fig. 6. Harbor problem grid and boundary conditions.

Non-reflecting boundary conditions are employed at the up-coast, down-coast, and off-shore boundaries which are noted in Fig. 6. Furthermore, the long-shore current is specified at the down-coast boundary, and the depth is specified on the off-shore boundary to generate long-waves in the model. Along the harbor boundary, the model enforces zero mass flux normal to the boundary.

Using a still-water initial condition, the model is integrated for 9 min and 40 s of real-time. Over this period of time, waves propagating towards the harbor are refracted by the sloping bed, diffract around and reflect off the harbor, and leave the domain through the up-coast and off-shore boundaries. The wave and velocity field at the final time is presented in Fig. 7. At this time, a periodic condition has been reached and a field of wave peaks and troughs is visible. The peaks and troughs visible in Fig. 7 represent the interference pattern between shoreward bound waves and the waves reflected off the harbor.

This application is hypothetical, but it highlights the performance of the boundary flux function presented here. Inspection of the off-shore, up-coast, and down-coast boundaries reveals a surface that takes on an oscillatory shape, even though the water level is specified uniformly. The oscillations are indicative of a boundary that is permitting waves from the interior to pass outwards while information for the interior of the solution is simultaneously being specified. It is also noteworthy that there is no amplification of wave energy near open boundaries, as might be expected in the presence of a reflective barrier. Instead, the image of the wave field

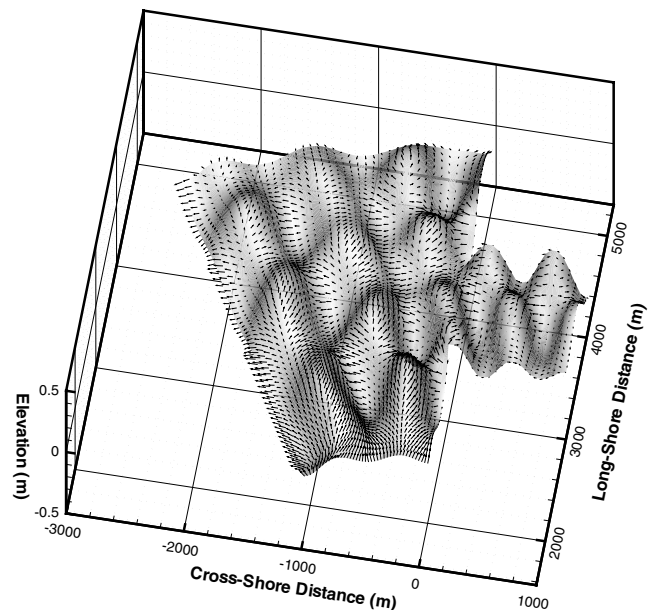


Fig. 7. Wave and velocity field in harbor problem. Waves advancing towards harbor are interfering with waves reflected off harbor. Image appears to be a subset of a solution on a much larger grid, but it is not.

appears as a subset of a much larger computation, even though it is not.

5. Conclusions

A non-reflecting flux function that can be easily implemented into a finite-volume shallow-water model is presented. The non-reflecting flux function should be used at open boundaries in shallow-water models where no physical control is present and the flow is subcritical. The boundary flux function allows information to be supplied to a solution domain while disturbances from within pass outwards unreflected.

Non-reflecting boundary conditions are implemented by interpreting the Riemann problem that exists at cell faces along open model boundaries as the interaction of two simple waves. This approximation to the Riemann problem facilitates the computation of fluxes at the boundary consistent with non-reflecting conditions, and it is straightforwardly implemented in the context of the MUSCL approach.

The non-reflecting boundary conditions yield near-perfect behavior when waves advance towards a boundary with a small incident angle (approximately less than 45°). Small reflections will occur when waves advance with a larger incident angle. In practical applications, the reflections would not constitute a significant modeling flaw.

Acknowledgements

The research leading to this paper was funded by the University of California Water Resources Center (Grant # W-908 and #W-942) whose support is gratefully acknowledged. The author is also appreciative of thought-provoking discussions with N. Katopodes and Y. Poon on matters related to this research.

References

- [1] Chaudhry MH. Open-channel flow. Englewood Cliffs, NJ: Prentice-Hall; 1993.
- [2] Verboom GK, Stelling GS, Officer MJ. Boundary conditions for the shallow-water equations. In: Abbott MB, Cunge JA, editors. Engineering applications of computational hydraulics, vol. 1. London: Pitman Advanced Publishing Program; 1982.
- [3] Alcudo F, Garcia-Navarro P, Saviron J-M. Flux difference splitting for 1D open channel flow equations. *Int J Num Meth Fluids* 1992;14:1009–18.
- [4] Alcudo F, Garcia-Navarro P. A high-resolution Godunov-type scheme in finite volumes for the 2D shallow-water equations. *Int J Num Meth Fluids* 1993;16:489–505.
- [5] Nuić M. Efficient implementation of non-oscillatory schemes for the computation of free-surface flows. *J Hyd Res* 1995;33:101–11.
- [6] Zhao DH, Lai JS, Shen HW. A finite volume two-dimensional unsteady flow model for river basins. *J Hyd Eng* 1994;120(7): 863–83.
- [7] Zhao DH, Shen HW, Lai JS, Tabios GQ. Approximate Riemann solvers in FVM for 2D hydraulic shock wave modeling. *J Hyd Eng* 1996;122(12):692–702.
- [8] Mingham CG, Causon DM. High-resolution finite-volume method for shallow-water flows. *J Hyd Eng* 1998;124(6): 605–14.
- [9] Causon DM, Mingham CG, Ingram DM. Advances in calculation methods for supercritical flow in spillway channels. *J Hyd Eng* 1999;125(10):1039–50.
- [10] Mingham CG, Causon DM. Calculation of unsteady bore diffraction using a high resolution finite-volume method. *J Hyd Res* 2000;38(1):49–56.
- [11] Sanders BF, Bradford SF. Computation of tidal co-oscillation in wetlands by finite-volume method. In: EM2000, Proceedings of the 14th Engineering Mechanics Conference, ASCE, Austin, 2000 (CD-ROM).
- [12] Bradford SF, Sanders BF. Finite-volume model for shallow water flooding and drying of arbitrary topography. *J Hyd Eng* 2002;128(3):289–98.
- [13] Engquist B, Majda A. Absorbing boundary conditions for the numerical simulation of waves. *Math Comput* 1977;31(139): 629–51.
- [14] Katopodes N, Strelkoff T. Two-dimensional shallow water-wave models. *J Eng Mech Div* 1979;105(EM2):317–34.
- [15] Henderson FH. Open channel flow. New York: Macmillan; 1966.
- [16] Hirsch C. Numerical computation of internal and external flows, vol. 2. New York: Wiley; 1990.
- [17] VanLeer B. Towards the ultimate conservative difference scheme. V. A second order sequel to Godunov's method. *J Comp Phys* 1979;32:101–36.
- [18] Bradford SF, Katopodes ND. Hydrodynamics of turbid underflows Part I: formulation and numerical analysis. *J Hyd Eng* 1999;125:1006–15.
- [19] Roe PL. Approximate Riemann solvers, parameter vectors, and difference schemes. *J Comp Phys* 1981;43:357–72.
- [20] Glaister P. Approximate Riemann solutions of the shallow water equations. *J Hyd Res* 1988;26(3):293–306.
- [21] Van Leer B, Lee WT, Powell KG. Sonic point capturing. In: AIAA 9th Computational Fluid Dynamics Conference, Buffalo, NY, 1989.
- [22] Poon, Y., Personal communication, 1999.